

Article

Photocatalytic Degradation of Methylene Blue over TiO₂ Pretreated with Varying Concentrations of NaOH

Chentao Hou * , Bo Hu and Jiaming Zhu 

College of Geology and Environment, Xi'an University of Science and Technology, Xi'an 710054, China; hubo920216@163.com (B.H.); XRD610@126.com (J.Z.)

* Correspondence: houct@xust.edu.cn; Tel.: +86-029-8558-3188

Received: 29 September 2018; Accepted: 15 November 2018; Published: 22 November 2018



Abstract: In this paper, different NaOH concentrations (2, 5, 10, and 15 M) were used to treat {001}TiO₂. The effect of NaOH on the crystal structure, morphology, optical properties, light raw electronic-hole recombination, and degradation performance of {001}TiO₂ on methylene blue were studied. The results demonstrate that rutile TiO₂ appeared when the NaOH concentration was as high as 10 M, showing much better photolytic performance than others. As the concentration of sodium hydroxide increases, the morphology changes accordingly. The specific surface area increases and the optical electronic-hole recombination rate decreases. Radical scavenging tests showed that hydroxyl radical and hole are very important in photocatalysis.

Keywords: {001}TiO₂; NaOH concentration; photocatalysis; radical scavenging; methylene blue

1. Introduction

Photocatalytic degradation oxidizes complex organic compounds into small molecular inorganic substances, such as carbon dioxide and water, under light. The reaction is thorough and causes no secondary pollution [1,2].

Methylene blue is used not only to dye paper and office supplies but also to tone up silk colors. It has largely been used in human and veterinary medicine for several therapeutic and diagnostic procedures. It cannot be degraded through the conventional water treatment process due to its complex aromatic structures, hydrophilic nature, and high stability against light, temperature, water, chemicals, etc., and it may cause substantial environment pollution.

Photocatalytic oxidation is considered to be one of the most effective ways of degrading methylene blue. A number of catalysts have been reported for methylene blue (MB) degradation over the past decade. A Pd-supported Cu-doped Ti-pillared montmorillonite catalyst was synthesized for MB degradation [3], and modified TiO₂/BiVO₄ photocatalysts were found to be active in the degradation of MB [4]. Mn-doped ZrO₂ nanoparticles [5], an MgO-SC_{CA-Zn} hybrid ozonation catalyst [6], Fe₃O₄/TiO₂ core/shell nanocubes [7], magnetic SrFe₁₂O₁₉ [8], ZnO/NiFe₂O₄ nanoparticles [9], Co-Mn-Fe complex oxide catalysts [10], CdS nanowire [11], silver nanoparticle decorated polymeric spheres [12], and Au/ZnO-CeO₂ [13] have been reported for MB degradation.

Due to its non-toxic, stable quality, and low price [14,15], TiO₂ has been shown to be the most effective photocatalyst in environmental pollution treatment [16], energy storage [17], biological applications [18], and dye solar cells [19]. However, TiO₂ can only be excited through ultraviolet lighting, accounting for only 2–4% of the solar spectrum and has a low utilization rate [20]. In addition, the high composite rate of photogenic electron holes greatly reduces its degradation efficiency, which significantly limits its practical application [21,22].

As a result, many scientists strive to reduce the width of the band gap and to lower the light electrons and holes of TiO₂ through composite metals (Cu [23], Ag [24], Au [25], and Ni [26]), non-metals (N [27], reductive graphene [28], carbon nanotubes [29], etc.), and other semiconductors (CdS [30], MoS₂ [31], WO₃ [32], C₃N₄ [33], etc.) with TiO₂ to improve its photocatalytic oxidation or reduction capability. The proportion of highly active surfaces also affects its catalytic properties. Research has shown that the photocatalytic oxidation {001} facet of anatase titanium dioxide is better than that of the {101} facet, while the surface energy of the {001} plane (0.90 J/m²) is greater than that of the {101} plane (0.44 J/m²) [34]. Therefore, anatase crystal is mainly composed of the thermodynamic stability of the {101} crystal form [35,36]. Yang presented a 47% exposure of the {001} crystal TiO₂ catalyst with titanium tetrachloride as the precursor and hydrofluoric acid as the growth control agent in 2008 [37], and scientists strive to improve its catalytic performance through composite Ag [38], SnS₂ [39], Bi₂WO₆ [40], MoS₂ [41] etc., but there is so far no report on varying concentrations toward {001}TiO₂.

In this paper, the effect of NaOH on the crystal structure, morphology, optical properties, light raw electronic-hole recombination and degradation performance of {001}TiO₂ on methylene blue (MB) was studied. Radical scavenging experiments were also investigated to identify active radicals.

2. Results

2.1. Structural Characterization

In Figure 1, it can be seen that the sample with the absence of NaOH (0 M) showed peaks at 25.28°, 37.80°, 48.04°, 53.89°, 55.06°, 62.68°, 70.31°, and 75.03°, indicating high purity anatase TiO₂ (JCPDS No. 21-1272). When the concentration of NaOH increased to 10 and 15 M, the peak at 27.24° appeared, indicating the appearance of rutile TiO₂ (JCPDS No. 21-1276). Meanwhile, the peaks are wider with the increase concentration of NaOH, indicating the crystallinity of the samples became poorer. The 15 M sample has the worst crystallinity among them.

Table 1 is the rutile content of each catalyst. The formula is as follows:

$$X_R = \frac{1}{1 + 0.8 \times \frac{I_A}{I_R}}$$

where X_R is rutile content; I_A is anatase {101} peak intensity; I_R is rutile {110} peak intensity. It was found that the rutile contents of 10 and 15 M are 43.48% and 52.91%, respectively.

Table 1. Rutile content of catalysts.

Samples	I_R ($2\theta = 27.24^\circ$)	I_A ($2\theta = 25.28^\circ$)	X_R
0 M	-	307.87	-
2 M	-	233.31	-
5 M	-	176.88	-
10 M	69.36	112.84	43.48%
15 M	69.09	76.83	52.91%

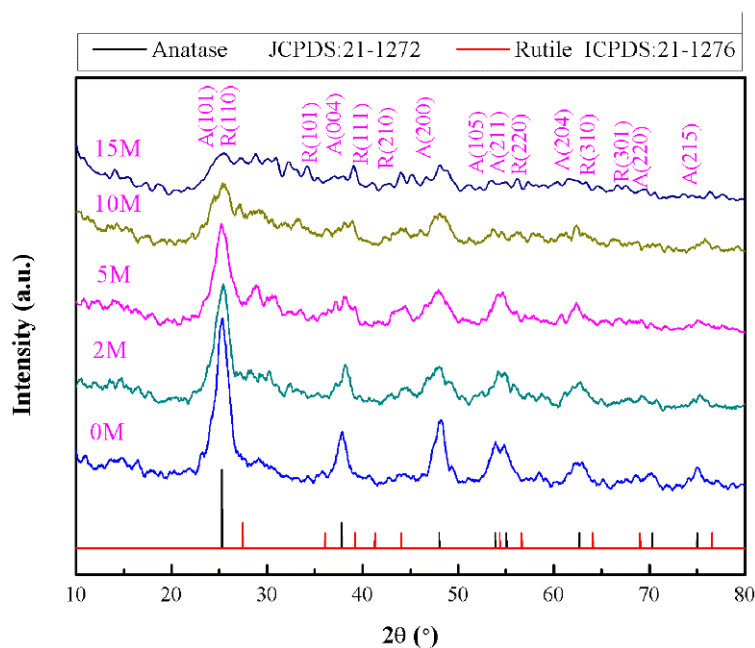


Figure 1. XRD patterns of as-prepared samples.

2.2. Lattice Spacing Analysis

Figure 2 presents the lattice spacing of the 0 and 10 M samples, respectively. Figure 2a shows that $d = 0.352$ nm and $d = 0.235$ nm, corresponding the {101} and {001} surface of the anatase titanium dioxide, respectively, which indicates that the synthesized catalyst is {001} titanium dioxide; in Figure 2b, it can be seen that the catalyst treated with 10 M NaOH not only has a {101} and {001} surface of anatase titanium but also has a {110} surface of rutile titanium (where $d = 0.324$ nm). Therefore, the catalyst treated with 10 M NaOH is anatase and rutile-mixed crystal, which is consistent with the XRD results.

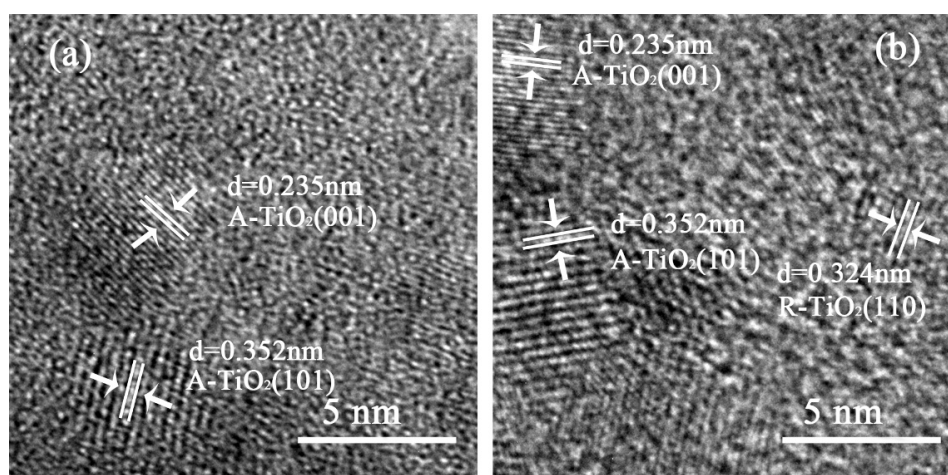


Figure 2. HRTEM diagram of catalyst: (a) 0 M; (b) 10 M.

2.3. Optical Performance

As can be seen in Figure 3, the intensity absorption of the sample in the visible light region is not as strong as that of the sample without the effect of NaOH, indicating that the absorption of light after NaOH treatment is not enhanced by NaOH.

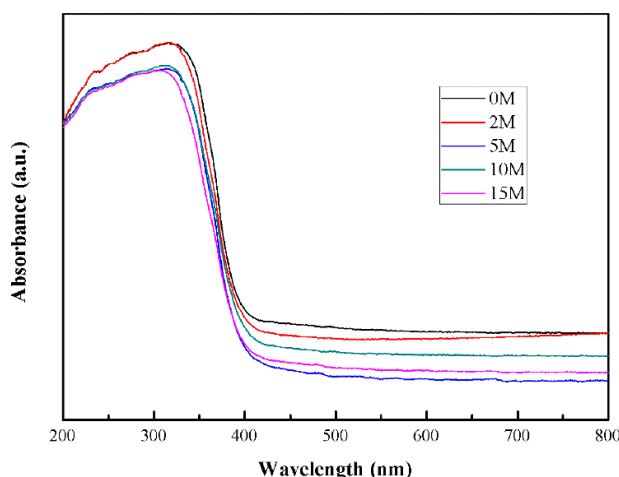


Figure 3. Optical absorption spectra of catalysts.

2.4. Crystal Morphology Analysis

As can be seen in Figure 4a, when NaOH is not added, the size of the sample is essentially the same and it is dispersed uniformly. In Figure 4b, it can be seen that it is made up of a rough ellipsoid on the surface. Figure 4c demonstrates that the sample after 2 M NaOH treatment is dispersed evenly, but the size is different, and in Figure 4d it can be seen that the morphology has been transformed from a rough surface to a smooth irregular shape. Figure 4e shows that the sample after the 5 M NaOH treatment has a slight reunion. Figure 4f shows that the sample size is different and the surface is smooth and irregular. In Figure 4g, it can be seen that the sample change after the 10 M NaOH treatment is light. Concerning the micro agglomeration phenomenon. Figure 4h shows that the size of the sample particles is significantly reduced; they are connected to each other through a number of network hubs, and there are more holes between them. These holes will provide more active sites for the follow-up reaction. Figure 4i shows that, after the 15 M NaOH treatment, the samples still have a slight reunion. As shown in Figure 4j, the size of the sample is different and the morphology is divided into flower grades. The interlaced structure provides an abundant surface area for the catalyst. In conclusion, with the increase in the NaOH concentration, the catalyst appears to have a slight reunion. At a low concentration (2 and 5 M), the surface of the catalyst is smooth, and the pore size of the catalyst (10 and 15 M) becomes rich at a high concentration (10 and 15 M).

2.5. BET Analysis

The pore size distribution and pore volume were analyzed using the Barrett–Joyner–Halenda (BJH) method, and the surface area was calculated using the Brunauer–Emmett–Teller (BET) method. Figure 5a demonstrates that the 0, 2, 5, 10, and 15 M samples all show a typical IV type N_2 adsorption–desorption isotherm and a significant opening of the hysteresis loops was observed for all samples, indicating developed mesopores [42]. The adsorption amounts of the samples rose with the increase to high P/P_0 , where multilayer adsorption occurred. Furthermore, for 10 M, a sharp increase in the adsorption amount in the P/P_0 range of 0.8–1.0 and a more significant opening of the hysteresis loop were observed, indicating stronger multilayer adsorption and better developed mesopores [43]. Considering the data in Table 2, the specific surface area of 0 and 15 M was small and not conducive to the adsorption of methylene blue. The specific surface area of 2 and 5 M was large, but the pores were too small and not conducive to macromolecular methylene blue adsorption. The best conduction was in the 10 M sample, and this construction may be attributed to its characteristics of mixed crystals.

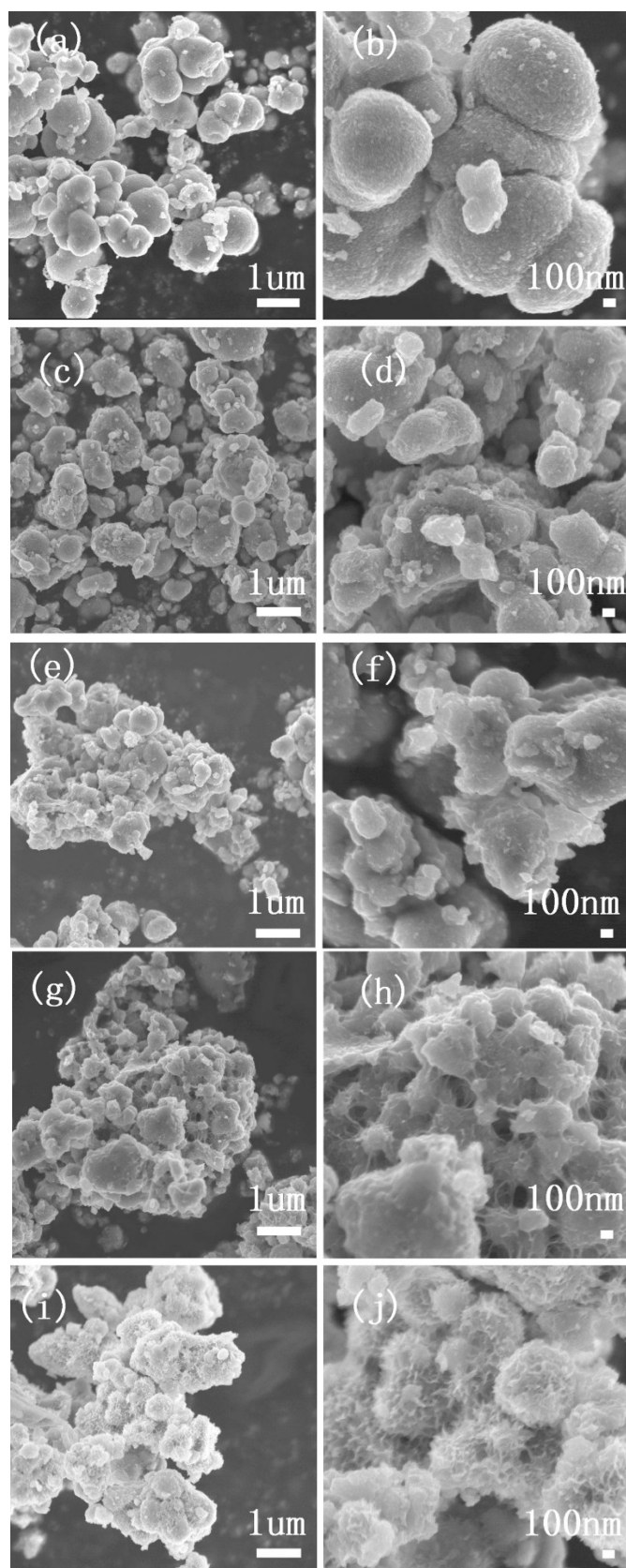


Figure 4. SEM images of the as-prepared samples: (a,b) 0 M; (c,d) 2 M; (e,f) 5 M; (g,h) 10 M; (i,j) 15 M.

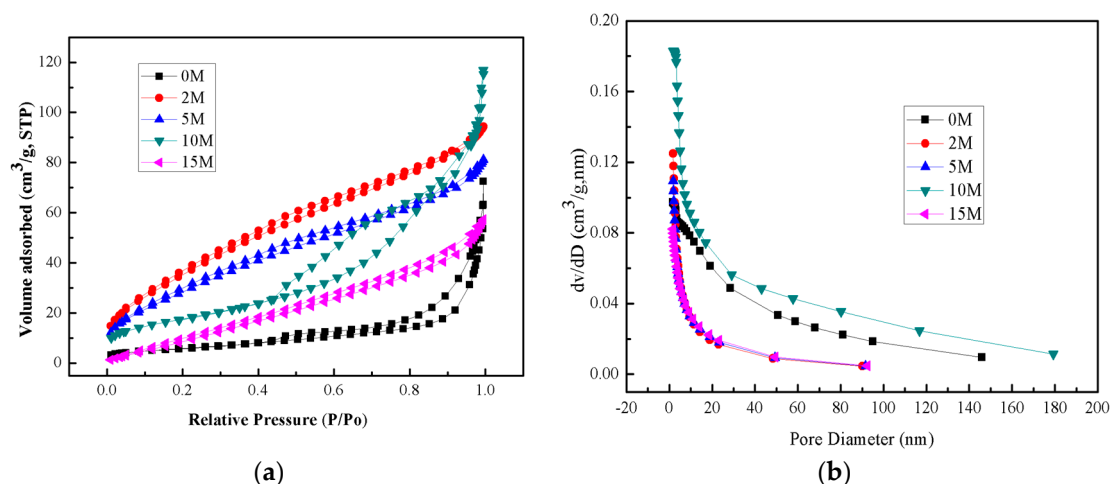


Figure 5. (a) N₂ adsorption–desorption isotherm of as-prepared samples; (b) pore diameter of the as-prepared samples.

Table 2. Physicochemical properties of samples.

Samples	BET Surface Area (m ² /g)	Pore Volume (cm ³ /g)	Pore Size (nm)
0 M	21.31	0.08	14.73
2 M	136.19	0.14	4.22
5 M	109.25	0.12	4.50
10 M	63.65	0.16	10.14
15 M	45.65	0.09	7.48

2.6. FT-IR Analysis

Figure 6 is the Fourier infrared image of the samples. The broad absorptions centered around 3396 and 2919 cm⁻¹ were, respectively, ascribed to the hydroxyl free radicals and the associated hydrogen bonds, and the peak around 1618 cm⁻¹ was attributed to the absorption of the water molecule [44]; the peak around 1300 cm⁻¹ was attributed to the in-plane bending vibration of OH bond, and the peak near 548 cm⁻¹ was caused by the absorption of Ti–O–Ti [45].

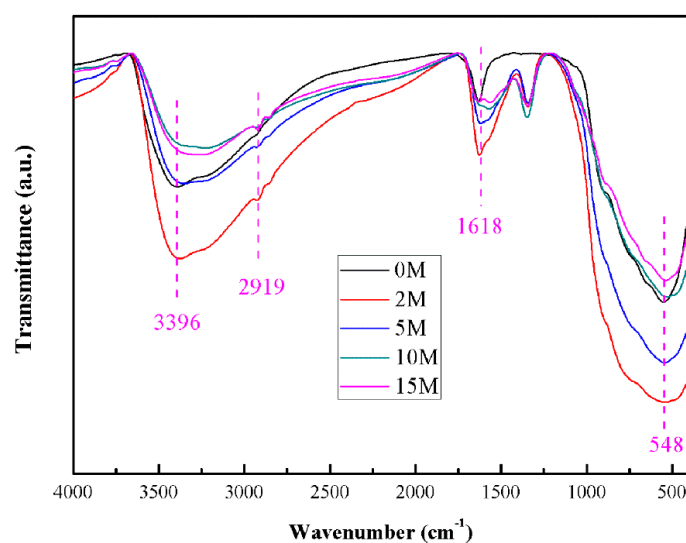


Figure 6. Fourier transform infrared (FT-IR) spectra of as-prepared samples.

2.7. Photoluminescence Analysis

Figure 7 presents the fluorescence spectrum of the XM series of catalysts. The fluorescence intensity in the fluorescence emission spectrum of a semiconductor photocatalyst can be used to characterize the recombination of photogenerated electrons and photogenerated holes; the lower the fluorescence intensity of the photogenerated electrons, the more effective the separation of the photogenerated cavitation [46]. It can be seen that the photogenerated electrons and holes in the catalyst after the 2 M NaOH treatment were easily compounded, and the photogenerated electrons and holes of the catalyst after 5, 10, and 15 M NaOH treatment, especially after 10 M NaOH treatment, were not easily compounded compared to the 0 and 2 M catalysts, which will greatly enhance the ability of the catalyst to degrade the contaminants.

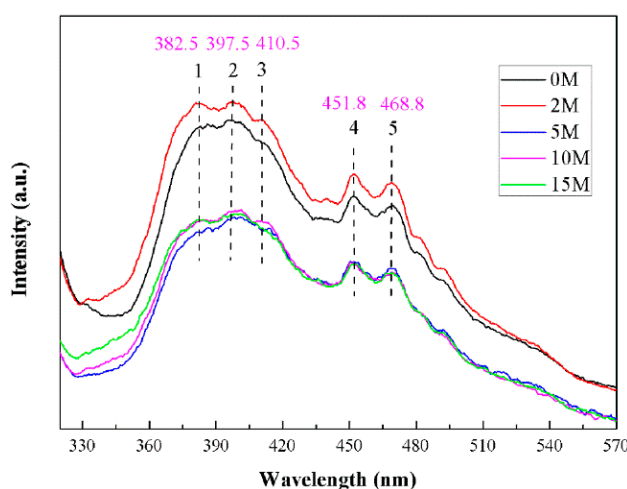


Figure 7. Photoluminescence (PL) emission spectra of as-prepared samples.

Five peaks were observed in the spectra. The broad emission bands centered at 382.5 nm (Peak 1), 397.5 nm (Peak 2), and 410.5 nm (Peak 3) were ascribed to the formation of boundaries of exciton emission due to the trapping of free excitons by the titanite groups near the defects. The long wavelength range of 451.8–468.8 nm (Peaks 4 and 5) is attributed to the oxygen vacancy with two trapped electrons. Oxygen vacancy sites are important for the formation of superoxide (O_2^-) and hydroxyl (OH) radicals for photocatalytic degradation [47].

2.8. Photocatalytic Activity

The degradation diagram of the prepared samples for methylene blue can be seen in Figure 8. It can be seen in Figure 8a that, when there was no photocatalyst without light (Dark, no catalyst), when there was only light (Light, catalyst), and when there was no catalyst (No catalyst), the concentration of methylene blue almost did not change, indicating that the properties of methylene blue are more stable. When catalysts were added, however, the concentration decreased dramatically, indicating that the reduction in methylene blue is a photocatalytic path. When the catalysts were treated with NaOH (2, 5, 10, and 15 M), the degradation performance was obviously improved. The best performance could be seen with the 10 M NaOH treatment. Figure 8b shows the degradation of 10 M methylene blue with different amounts of 10 M. When the amount of catalyst was 5 and 10 mg, respectively, it could not contact with the methylene blue molecule sufficiently, resulting in an unobvious degradation of methylene blue. The 10 M catalyst of 20 mg not only has a strong adsorption capacity to the methylene blue molecule, but also shows excellent photodegradation performance. The 30 and 50 mg 10 M catalysts were sufficient to make most of the methylene blue in the dark reaction stage. The subsurface of the catalyst was adsorbed on the surface of the catalyst, showing the excellent adsorption properties of the catalyst, which means that the photodegradation performance

was not outstanding. Figure 8c shows the UV-vis absorption spectral changes of the 20 mg 10 M sample. It can be seen that methylene blue had two absorption peaks at 256 and 665 nm. The UV-vis absorption could detect the oxidation of methylene blue; at the same time, we observed that the color of the methylene blue gradually became colorless from dark blue, indicating that methylene blue was gradually oxidized. Figure 8d presents the free radical scavenging results. Potassium iodide and hole were reduced by the free radical (OH) binding of terephthalic acid to the hydroxyl group (h^+). The activity of the catalyst was reduced. The quinone could be combined with a superoxide free radical (O_2^-) to reduce the activity of the catalyst. When the methylene blue was degraded, the addition of quinone was obviously better than the addition of potassium iodide and terephthalic acid, indicating that hydroxyl radicals and holes play a leading role in photocatalysis.

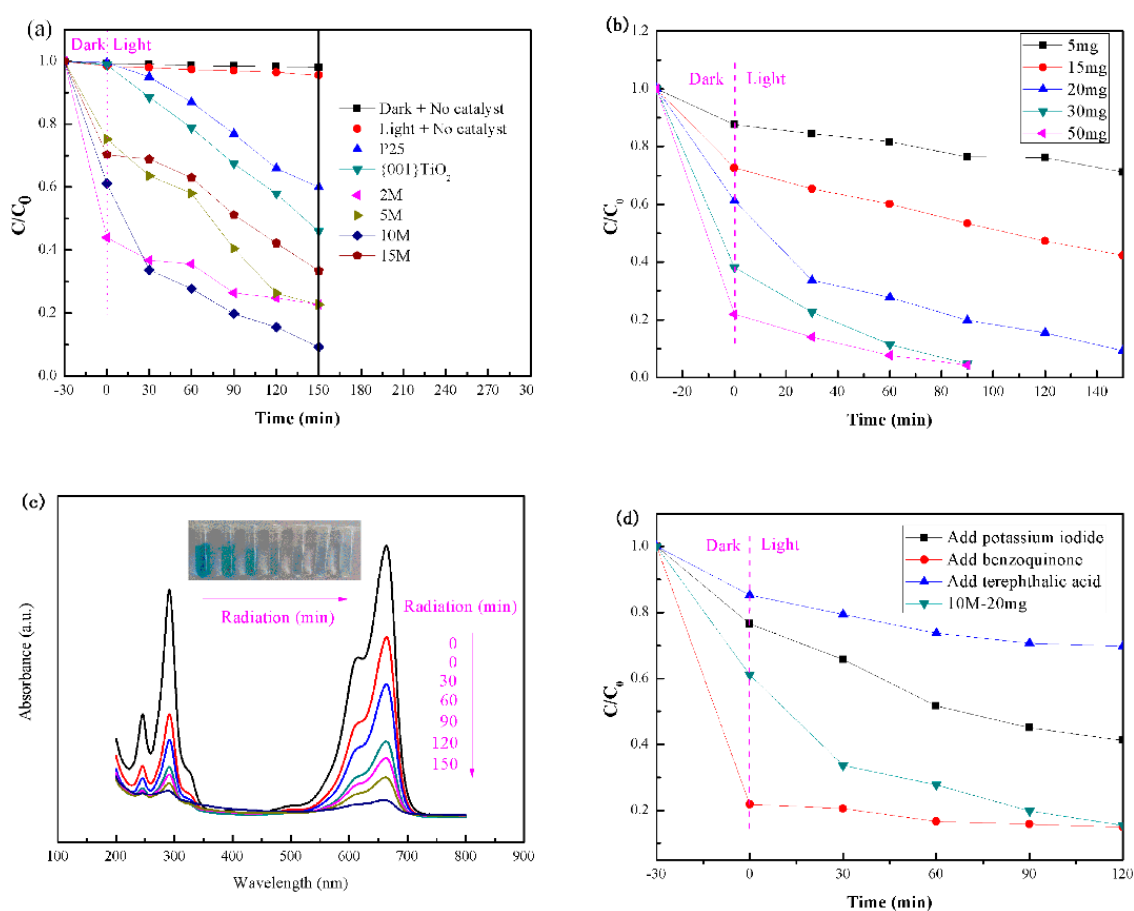


Figure 8. Degradation diagram of the prepared samples for methylene blue. (a) Photocatalytic performance of MB samples; (b) the effect of the different amount of 10 M samples on methylene blue; (c) UV-vis absorption spectral changes with photocatalytic degradation time of MB with the 20 mg 10 M sample; (d) radical-scavenging experiments of the 10 M sample.

3. Discussion

From the above results, after NaOH treatment, the crystal shape of the anatase F-TiO₂ samples changed. In particular, when the concentration of NaOH increased to 10 and 15 M, rutile TiO₂ appeared, while the crystallinity of the 15 M samples was poor compared to the other samples. This was confirmed by the HRTEM results. Considering the UV-vis diffuse reflectance and FTIR spectra of the samples, NaOH treatment did cause a bandgap and surface bonds changes, but these did not lead to the best performance of the 10 M sample. The BET and PL data revealed that the 10 M sample had the best adsorption potentiality and that its recombination of photogenerated electrons and photogenerated holes was the most inhibited.

Therefore, the reason why the 10 M sample showed the best performance may be that it has the best adsorption potentiality and can adsorb more MB onto its surface. It comprises rutile and anatase mixtures, too, whose recombination of photogenerated electrons and photogenerated holes is most inhibited; therefore, more electrons can react with the dissolved oxygen molecules to yield superoxide radical anions (O_2^-) [48]. MB can also be decomposed by holes directly [47]. This is in accordance with the radical scavenging experiments.

4. Materials and Methods

4.1. Materials

Materials used are as follows: butyl titanate, 1–4 of benzoquinone (AR, Chengdu Cologne Chemical Co., LTD., Chengdu, China), anhydrous ethanol (AR, Chongqing in East Sichuan Chemical Co., LTD., Chongqing, China), hydrofluoric acid (AR, Sichuan West Long Chemical Co., LTD., Chengdu, China), P25 (Degussa) and methylene blue (AR, Guangzhou Jinhua Large Chemical Reagent Co., LTD., Guangzhou, China), sodium hydroxide (AR, Chengdu xindu OuMuLan town industrial development zone), terephthalic acid (AR, Shanghai McLean Biological Co., LTD., Shanghai, China), and potassium iodide (AR, Chemical Engineering and Technology Research and Development Center of Guangdong Province). Ultrapure water (18.2 M Ω cm) was used as water all the experiments.

4.2. Preparation of Catalysts

A total of 15.20 mL of anhydrous ethanol was added to 17.60 mL of butyl titanate, which was denoted as Solution A. A total of 15.20 mL of anhydrous ethanol was added to 90 mL of distilled water and 6 mL of HF was added at the same time, denoted as Solution B. Solution A was added to Solution B dropwise, 4 drops per second, and mixed at a low speed for 2 h. The TiO₂ gel was obtained and aged at room temperature for 24 h. The aged gel was removed to a stainless-steel reaction kettle containing a PTFE bladder 100 °C for 2 h, then cooled and centrifugal sedimented. The sediment was washed three times with ultrapure water and ethanol and then dried at 100 °C in a drum wind drying oven. The as-prepared powder was F-TiO₂.

An amount of 1.5 g of TiO₂ was added to 100 mL of 0, 2, 5, 10, and 15 M sodium hydroxide solution for 100 min, and the powder was centrifugally sedimented, washed with ultrapure water three times, and dried in a 100 °C drum wind drying oven; the as-prepared powder was denoted as XM (X = 2, 5, 10, 15). We marked the untreated samples as {001}TiO₂ or 0 M.

4.3. Catalyst Characterization

The crystal structure was analyzed using an XD-2 X-ray diffractometer (Beijing Purkinje, Beijing, China) with Cu K α radiation. The morphology was examined using SEM (JEOL JSM6700, Tokyo, Japan) and high-resolution transmission electron microscopy (HRTEM; Tecnai G2 F20, FEI, Hillsborough, OR, USA) with an accelerating voltage of 200 kV. The specific surface area and porosimetry were measured using Micromeritic TriStar II 3020 micrometrics (Micromeritics, Norcross, GA, USA), and the BET method was used to calculate the surface area (S_{BET}). Fourier transform infrared (FT-IR) spectra were recorded using a TENSOR27 (Bruker, Frankfurt, Germany). The optical properties were determined using UV-vis diffuse reflectance spectroscopy (UV-vis DRS; Shimadzu 2600, Kyoto, Japan). Photoluminescence (PL) emission spectra were measured at room temperature with a fluorescence spectrophotometer (Hitachi F-2700, Tokyo, Japan) using a 325 nm line with an Xe lamp.

4.4. Photocatalytic Activity Tests

The prepared catalyst was used to degrade MB under a xenon lamp located at a distance of approximately 20 cm at 300 W, and its photocatalytic performance was studied through comparison with P25. Photocatalytic samples of 20 mg were added to 100 mL of a 10 mg/L of MB solution, and magnetic stirred for 0.5 h in the dark to obtain the adsorption–desorption balance, and the xenon

lamp was then opened. A 5 mL of the solution was taken out every 0.5 h and centrifuged at a high speed of 10,000 r/min, and the supernatant was tested using a UV1901 UV-vis spectrophotometer in 665 nm, with distilled water as a contrast. The concentration of MB was calculated according to Lambert–Beer’s law. The photocatalytic efficiency was

$$\eta(100\%) = C/C_0 \times 100\% = A/A_0 \times 100\%$$

where C_0 is the concentration before the reaction, and C is the concentration obtained using centrifugation every 30 min during the reaction. A_0 is the absorbance before the reaction, and A is the absorbance obtained using centrifugation every 30 min during the reaction.

4.5. Radical Scavenging Experiment

Potassium iodide (3 mmol/L), terephthalic acid (3 mmol/L), and quinone (3 mmol/L) were added to the 10 M degradation system, respectively, to catch OH, h^+ , and O_2^- .

5. Conclusions

In this paper, {001}TiO₂ catalysts with different morphologies were treated with different NaOH concentrations. After different NaOH concentrations were added, the photocatalyst was generally not improved in terms of optical properties; the 2 M photocatalyst had a high photoelectron hole recombination rate. The 10 and 15 M catalysts had a larger surface area and a low photoelectron hole recombination rate. Rutile was produced during the formation of the 10 M crystals. The experimental results showed that the 10 M catalyst contained anatase and rutile-mixed crystal and had a high activity {001} surface, resulting in the best degradation effect. This shows that the appropriate NaOH concentration {001}TiO₂ can not only change characterization but can also improve degradation performance. The amount of catalyst plays an important role in the entire process of methylene blue degradation. The 10 M catalyst of 20 mg is mainly photocatalytic to methylene blue degradation; when the amount of catalyst is 30 mg, the concentration of methylene blue is mainly reduced through adsorption. The free radical scavenging experiment showed that hydroxyl radicals and holes play a leading role in photocatalysis.

Author Contributions: C.H. and J.Z. designed the experiments; H.B. conducted the experiments; All authors analyzed the data; C.H. wrote the article.

Acknowledgments: This research was funded by [Shaanxi Key Industrial Projects] [2014GY2-07] and [the Science and Technology Research Plan] [15JK1460].

Conflicts of Interest: There is no conflict of interests existing in the manuscript submission, and it is approved by all of the authors for publication. All the authors listed have approved the manuscript to be enclosed.

References

1. Ochiai, T.; Fujishima, A. Photoelectrochemical properties of TiO₂ photocatalyst and its applications for environmental purification. *Photochem. Photobiol.* **2012**, *13*, 247–262. [[CrossRef](#)]
2. Wang, Y.F.; Tao, J.J.; Wang, X.Z.; Wang, Z.; Zhang, M.; Gang, H.; Sun, Z.Q. A unique Cu₂O/TiO₂ nanocomposite with enhanced photocatalytic performance under visible light irradiation. *Ceram. Int.* **2017**, *43*, 4866–4872. [[CrossRef](#)]
3. Joseph, N.; Vellayan, K.; González, B.; Vicente, M.A.; Gil, A. Effective degradation of methylene blue in aqueous solution using Pd supported Cu-doped Ti-pillared montmorillonite catalyst. *Appl. Clay Sci.* **2019**, *168*, 7–10. [[CrossRef](#)]
4. Samsudin, M.F.; Sufian, S.; Bashiri, R.; Mohamed, N.M.; Siang, L.T.; Ramli, R.M. Optimization of photodegradation of methylene blue over modified TiO₂/BiVO₄ photocatalysts: Effects of total TiO₂ loading and different type of co-catalyst. *Mater. Today Proc.* **2018**, *5*, 21710–21717. [[CrossRef](#)]
5. Khaksar, M.; Amini, M.; Boghaei, D.M.; Chae, K.H.; Gautam, S. Mn-doped ZrO₂ nanoparticles as an efficient catalyst for green oxidative degradation of methylene blue. *Catal. Commun.* **2015**, *72*, 1–5. [[CrossRef](#)]

6. Kong, L.; Diao, Z.; Chang, X.; Chen, D. Synthesis of recoverable and reusable granular MgO-SC_{CA-Zn} hybrid ozonation catalyst for degradation of methylene blue. *J. Environ. Chem.* **2016**, *4*, 4385–4391. [[CrossRef](#)]
7. Abbas, M.; Rao, B.P.; Reddy, V.; Kim, C. Fe₃O₄/TiO₂ core/shell nanocubes: Single-batch surfactantless synthesis, characterization and efficient catalysts for methylene blue degradation. *Ceram. Int.* **2014**, *40*, 11177–11186. [[CrossRef](#)]
8. Mishra, D.D.; Tan, G. Visible photocatalytic degradation of methylene blue on magnetic SrFe₁₂O₁₉. *J. Phys. Chem. Solids* **2018**, *123*, 157–161. [[CrossRef](#)]
9. Adeleke, J.T.; Theivasanthi, T.; Thiruppathi, M.; Swaminathan, M.; Akomolafe, T.; Alabi, A.B. Photocatalytic degradation of methylene blue by ZnO/NiFe₂O₄ nanoparticles. *Appl. Surf. Sci.* **2018**, *455*, 195–200. [[CrossRef](#)]
10. Huang, D.; Ma, J.; Fan, C.; Wang, K.; Zhao, W.; Peng, M.; Komarneni, S. Co-Mn-Fe complex oxide catalysts from layered double hydroxides for decomposition of methylene blue: Role of Mn. *Appl. Clay Sci.* **2018**, *152*, 230–238. [[CrossRef](#)]
11. Ganesh, R.S.; Durgadevi, E.; Navaneethan, M.; Sharma, S.K.; Binitha, H.S.; Ponnusamy, S.; Muthamizhchelvan, C.; Hayakawa, Y. Visible light induced photocatalytic degradation of methylene blue and rhodamine B from the catalyst of CdS nanowire. *Chem. Phys. Lett.* **2017**, *684*, 126–134. [[CrossRef](#)]
12. Liao, G.; Li, Q.; Zhao, W.; Pang, Q.; Gao, H.; Xu, Z. In-situ construction of novel silver nanoparticle decorated polymeric spheres as highly active and stable catalysts for reduction of methylene blue dye. *Appl. Catal. A Gen.* **2018**, *549*, 102–111. [[CrossRef](#)]
13. Veziroglu, S.; Kuru, M.; Ghorji, M.Z.; Dokan, F.K.; Hinz, A.M.; Strunskus, T.; Faupel, F.; Aktas, O.C. Ultra-fast degradation of methylene blue by Au/ZnO-CeO₂ nano-hybrid catalyst. *Mater. Lett.* **2017**, *209*, 486–491. [[CrossRef](#)]
14. Ali, W.; Jaffari, G.H.; Khan, S.; Liu, Y. Morphological control of 1D and 3D TiO₂ nanostructures with ammonium hydroxide and TiO₂ compact layer on FTO coated glass in hydrothermal synthesis. *Mater. Chem. Phys.* **2018**, *214*, 48–55. [[CrossRef](#)]
15. Sasahar, A.; Murakami, T.; Tu, L.T.U.; Tomitori, M. Nanoscale characterisation of TiO₂(110) annealed in air. *Appl. Surf. Sci.* **2018**, *428*, 1000–1005. [[CrossRef](#)]
16. Zhang, Q.; Fu, Y.; Wu, Y.; Zhang, Y.N.; Zuo, T. Low-cost Y-doped TiO₂ nanosheets film with highly reactive {001} facets from CRT waste and enhanced photocatalytic removal of Cr(VI) and methyl orange. *ACS Sustain. Chem. Eng.* **2016**, *4*, 1794–1803. [[CrossRef](#)]
17. Zhao, J.; Yang, Y.Y.; Li, Y.; Zhao, L.; Wang, H.; Song, G.L.; Tang, G.Y. Microencapsulated phase change materials with TiO₂-doped PMMA shell for thermal energy storage and UV-shielding. *Sol. Energy Mater. Sol. Cells* **2017**, *168*, 62–68. [[CrossRef](#)]
18. Endres, P.J.; Tatjana, P.; Stefan, V.; Meade, T.J.; Woloschak, G.E. DNA-TiO₂ nanoconjugates labeled with magnetic resonance contrast agents. *J. Am. Chem. Soc.* **2007**, *129*, 15760–15761. [[CrossRef](#)] [[PubMed](#)]
19. Fitra, M.; Daut, I.; Irwanto, M.; Gomes, N.; Irwan, Y.M. Effect of TiO₂ thickness dye solar cell on charge generation. *Energy Procedia* **2013**, *36*, 278–286. [[CrossRef](#)]
20. Pu, S.H.; Long, D.B.; Liu, Z.H.; Yang, F.Y.; Zhu, J.M. Preparation of RGO-P25 Nanocomposites for the Photocatalytic Degradation of Ammonia in Livestock Farms. *Catalysts* **2018**, *8*, 189. [[CrossRef](#)]
21. Zuo, S.; Jiang, Z.; Liu, W.; Yao, C.; Chen, Q.; Liu, X. Synthesis and Characterization of Urchin-like Mischcrystal TiO₂ and Its Photocatalysis. *Mater. Charact.* **2014**, *96*, 177–182. [[CrossRef](#)]
22. Ma, Q.L.; Zhang, H.X.; Cui, Y.Q.; Deng, X.Y.; Guo, R.N.; Cheng, X.W.; Xie, M.Z.; Cheng, Q.F. Fabrication of Cu₂O/TiO₂ nano-tube arrays photoelectrode and its enhanced photoelectrocatalytic performance for degradation of 2,4,6-trichlorophenol. *J. Ind. Eng. Chem.* **2018**, *57*, 181–187. [[CrossRef](#)]
23. Wei, C.; Wang, Y.H.; Liu, S.; Li, G.; Mao, L.Q.; Fan, Z.Y.; Shang, G.W.F.; Jiang, Z. Non-noble metal Cu as a cocatalyst on TiO₂ nanorod for highly efficient photocatalytic hydrogen production. *Appl. Surf. Sci.* **2018**, *445*, 527–534. [[CrossRef](#)]
24. Angkaew, S.; Limsuwan, P. Preparation of silver-titanium dioxide core-shell (Ag@TiO₂) nanoparticles: Effect of Ti-Ag mole ratio. *Procedia Eng.* **2012**, *32*, 649–655. [[CrossRef](#)]
25. Vipul, S.; Suneel, K.; Venkata, K. Shape Selective Au-TiO₂ Nanocomposites for Photocatalytic Applications. *Mater. Today Proc.* **2016**, *3*, 1939–1948. [[CrossRef](#)]
26. Barmeh, A.; Nilfroushan, M.R.; Otraj, S. Wetting and photocatalytic properties of Ni-doped TiO₂ coating on glazed ceramic tiles under visible light. *Thin Solid Films* **2018**, *666*, 137–142. [[CrossRef](#)]

27. Chen, Y.Z.; Li, A.X.; Li, Q.; Hou, X.M.; Wang, L.N.; Huang, Z.H. Facile fabrication of three-dimensional interconnected nanoporous N-TiO₂ for efficient photoelectrochemical water splitting. *J. Mater. Sci. Technol.* **2018**, *34*, 955–960. [[CrossRef](#)]
28. Zhang, G.Y.; Sun, Y.B.; Zhang, C.X.; Yu, Z.Q. Decomposition of acetaminophen in water by a gas phase dielectric barrier discharge plasma combined with TiO₂-rGO nanocomposite: Mechanism and degradation pathway. *J. Hazard. Mater.* **2017**, *323*, 719–729. [[CrossRef](#)] [[PubMed](#)]
29. Mohammad, B.A.; Zoha, T.B.; Majid, S.; Sedigheh, B.D.; Payam, V. Synthesis of TiO₂ nanoparticles and decorated multi-wall carbon nanotube (MWCNT) with anatase TiO₂ nanoparticles and study of optical properties and structural characterization of TiO₂/MWCNT nanocomposite. *Optik* **2017**, *149*, 447–454. [[CrossRef](#)]
30. Li, G.; Wu, L.; Li, F.; Xu, P.; Zhang, D.; Li, H. Photoelectrocatalytic degradation of organic pollutants via a CdS quantum dots enhanced TiO₂ nanotube array electrode under visible light irradiation. *Nanoscale* **2013**, *5*, 2118–2125. [[CrossRef](#)] [[PubMed](#)]
31. Zhou, W.; Yin, Z.; Du, Y.; Huang, X.; Zeng, Z.; Fan, Z.; Liu, H.; Wang, J.; Zhang, H. Synthesis of few-layer MoS₂ nanosheet-coated TiO₂ nanobelt heterostructures for enhanced photocatalytic activities. *Small* **2013**, *9*, 140–147. [[CrossRef](#)] [[PubMed](#)]
32. Yu, S.Q.; Ling, Y.H.; Wang, R.G.; Zhang, J.; Qin, F.; Zhang, Z.J. Constructing superhydrophobic WO₃@TiO₂ nanoflake surface beyond amorphous alloy against electrochemical corrosion on iron steel. *Appl. Surf. Sci.* **2018**, *436*, 527–537. [[CrossRef](#)]
33. Zhou, L.; Wang, L.Z.; Lei, J.Y.; Liu, Y.D.; Zhang, J.L. Fabrication of TiO₂/Co-g-C₃N₄ heterojunction catalyst and its photocatalytic performance. *Catal. Commun.* **2017**, *89*, 125–128. [[CrossRef](#)]
34. Mohamed, M.A.; Sandhya, K.Y. Selective photodegradation and enhanced photo electrochemical properties of titanium dioxide-graphene composite with exposed (001) facets made by photochemical method. *Sol. Energy Mater. Sol. Cells* **2016**, *144*, 748–757. [[CrossRef](#)]
35. Lazzeri, M.; Vittadini, A.; Selloni, A. Erratum: Structure and energetic of stoichiometric TiO₂ anatase surfaces. *Phys. Rev. B* **2002**, *65*, 1–5. [[CrossRef](#)]
36. Diebold, U. The surface science of titanium dioxide. *Surf. Sci. Rep.* **2003**, *48*, 53–229. [[CrossRef](#)]
37. Yang, H.G.; Sun, C.H.; Qiao, S.Z.; Zou, J.; Liu, G.; Smith, S.C.; Cheng, H.M.; Lu, G.Q. Anatase TiO₂ single crystals with a large percentage of reactive facets. *Nature* **2008**, *453*, 638–641. [[CrossRef](#)] [[PubMed](#)]
38. Zhang, Y.; Wang, T.; Zhou, M.; Wang, Y.; Zhang, Z.G. Hydrothermal preparation of Ag-TiO₂ nanostructures with exposed {001}/{101} facets for enhancing visible light photocatalytic activity. *Ceram. Int.* **2017**, *43*, 3118–3126. [[CrossRef](#)]
39. Zhang, J.; Zhang, L.L.; Shi, Y.X.; Xu, G.L.; Zhang, E.P.; Wang, H.B.; Zhe, K.; Xi, J.H.; Jia, Z.G. Anatase TiO₂ nanosheets with coexposed {101} and {001} facets coupled with ultrathin SnS₂ nanosheets as a face-to-face n-p-n dual heterojunction photocatalyst for enhancing photocatalytic activity. *Appl. Surf. Sci.* **2017**, *420*, 839–848. [[CrossRef](#)]
40. Zhang, J.; Huang, L.H.; Lu, Z.D.; Jin, Z.L.; Wang, X.Y.; Xu, G.L.; Zhang, E.P.; Wang, H.B.; Zhe, K.; Xi, J.H.; et al. Controllable synthesis of Bi₂WO₆(001)/TiO₂(001) heterostructure with enhanced photocatalytic activity. *J. Alloy. Compd.* **2016**, *676*, 37–45. [[CrossRef](#)]
41. Zhang, J.; Huang, L.H.; Lu, Z.D.; Jin, Z.L.; Wang, X.Y.; Xu, G.L.; Zhang, E.P.; Wang, H.B.; Zhe, K.; Xi, J.H.; et al. Crystal face regulating MoS₂/TiO₂(001) heterostructure for high photocatalytic activity. *J. Alloy. Compd.* **2016**, *688*, 840–848. [[CrossRef](#)]
42. Xiang, Q.J.; Lv, K.L.; Yu, J.G. Pivotal role of fluorine in enhanced photocatalytic activity of anatase TiO₂ nanosheets with dominant (001) facets for the photocatalytic degradation of acetone in air. *Appl. Catal. B Environ.* **2010**, *96*, 557–564. [[CrossRef](#)]
43. Nie, L.; Yu, J.; Li, X.; Cheng, B.; Liu, G.; Jaroniec, M. Enhanced Performance of NaOH-Modified Pt/TiO₂ toward Room Temperature Selective Oxidation of Formaldehyde. *Environ. Sci. Technol.* **2013**, *47*, 2777–2783. [[CrossRef](#)] [[PubMed](#)]
44. Hou, C.; Liu, W.; Zhu, J. Synthesis of NaOH-Modified TiOF₂ and Its Enhanced Visible Light Photocatalytic Performance on RhB. *Catalysts* **2017**, *7*, 243. [[CrossRef](#)]
45. Wang, H.; Yi, G.; Tan, M.; Zu, X.; Luo, H.; Jiang, X. Initial reactant controlled synthesis of double layered TiO₂ nanostructures and characterization of its spectra of absorption and photoluminescence. *Mater. Lett.* **2015**, *148*, 5–8. [[CrossRef](#)]

46. Park, H.; Choi, W. Photocatalytic Reactivities of Nafion-Coated TiO₂ for the Degradation of Charged Organic Compounds under UV or Visible Light. *J. Phys. Chem. B* **2005**, *109*, 11667–11674. [[CrossRef](#)] [[PubMed](#)]
47. Yuan, L.; Weng, B.; Colmenares, J.C.; Sun, Y.; Xu, Y.-J. Multichannel charge transfer and mechanistic insight in metal decorated 2D-2D Bi₂WO₆-TiO₂ cascade with enhanced photocatalytic performance. *Small* **2017**, *13*, 1702253. [[CrossRef](#)] [[PubMed](#)]
48. Hou, C.T.; Liu, W.L. One-step synthesis of OH-TiO₂/TiOF₂ nanohybrids and their enhanced solar light photocatalytic performance. *R. Soc. Open Sci.* **2018**, *5*, 172005. [[CrossRef](#)] [[PubMed](#)]



© 2018 by the authors. Licensee MDPI, Basel, Switzerland. This article is an open access article distributed under the terms and conditions of the Creative Commons Attribution (CC BY) license (<http://creativecommons.org/licenses/by/4.0/>).